metals

MDPI

Article

Irradiation-Assisted Microstructure Evolution and Mechanical Properties Loss of 310S Welded Joints

Yunlu Jiang [1,2], Ying Kan [1], Changzhong Wu [1] and Huaining Chen [1,*]

[1] CAS Key Laboratory of Nuclear Materials and Safety Assessment, Institute of Metal Research Chinese, Academy of Sciences, Shenyang 110016, China
[2] School of Materials Science and Engineering, University of Science and Technology of China, Shenyang 110016, China
* Correspondence: hnchen@imr.ac.cn

Abstract: In order to reveal the effect of irradiation damage caused by high-level liquid radioactive wastes on the welded joint of the container, the irradiation-induced microstructure evolution and mechanical properties degradation of the 310S stainless steel welded joints were investigated in this study. For this purpose, the 1.3 MeV ^{60}Co and 2 MeV accelerators were used to simulate irradiation experiments on 310S welded joints. The uniaxial tensile tests characterized the specimens' mechanical properties and fracture morphology. The results revealed that elongation was reduced by about 5% of irradiation damage by ^{60}Co, and the fracture morphology shows a large number of secondary cracks. In contrast, the elongation was recovered irradiated by the accelerator, and the fracture morphology showed a large number of dimples. Following the interrupted creep deformation, creep fracture tests were conducted for irradiation specimens. The ^{60}Co irradiation damage significantly decreases the creep resistance, leading to deformation of creep, which is increased to 1.5 times that of those unirradiated specimens. At the same time, the ductility is seriously degraded for the irradiated creep fracture specimens. As a result, the creep fracture strain of ^{60}Co specimens is reduced to 70% of that of unirradiated specimens. Further, ductility reduction was related to the irradiated hardening by ^{60}Co, while Nano-indenter hardness was 5.9 GPa, higher by 44% than the unirradiated specimens. The results are shown in an enrichment of Cr, C and P elements at phase boundaries for ^{60}Co irradiation specimens, while the magnitude of element segregation increased by the accelerator combination irradiation. Finally, the creep cracking analysis results show intergranular cracking was observed on the surfaces of the irradiated specimens, while the $M_{23}C_6$ has a primary relationship with the intergranular cracks. The synergic effect of irradiation promoted damage, and element segregation was the primary cause of the intergranular cracking of the 310S welded joints.

Keywords: 310S stainless steel; welded joints; irradiation damage; microstructure evolution; mechanical property

Citation: Jiang, Y.; Kan, Y.; Wu, C.; Chen, H. Irradiation-Assisted Microstructure Evolution and Mechanical Properties Loss of 310S Welded Joints. *Metals* **2023**, *13*, 858. https://doi.org/10.3390/met13050858

Academic Editor: António Bastos Pereira

Received: 22 March 2023
Revised: 20 April 2023
Accepted: 24 April 2023
Published: 28 April 2023

1. Introduction

With the operations and decommissioning of the nuclear facility, the production and accumulation of high-level liquid radioactive waste will increase yearly. Its safe storage and post-processing are essential to nuclear energy's sustainable, healthy and stable development [1]. The glass solidification process dominates in high-level radioactive waste post-processing [2]. AISI 310S austenitic stainless steel has been widely used in solidification containers and nuclear power plants due to its prominent radiation resistance and mechanical properties [3–5]. The solidification containers filling the high-level liquid radioactive will pose irradiation damage for heterogeneous microstructure welded joints. The high-level irradiation damage could cause undesirable property changes for welded joints, such as hardening, embrittlement, loss of ductility, fracture toughness decrease and local chemical variations radiation-induced segregation (RIS) [6,7]. Irradiation-induced

mechanical properties degradation and microstructure evolution are required for life prediction and demand security management during service [8]. Accurately forecasting irradiation damage could evaluate the dimensional stability and potential risk of the life extension for the container. Reviews of the damage of austenitic stainless steel welded joint's mechanical properties under irradiation conditions can be described as the irradiation-induced microstructure features, such as precipitates, dislocation loops and elements segregation [9,10]. Microstructure evolution is strongly linked to mechanical properties damage. Recent research of irradiated structural components stainless steel welded joints serviced in the irradiated environment has higher intergranular cracking susceptibility in laboratory confirmation [11–13]. Meanwhile, irradiation-induced hardening was identified as a main detrimental factor of the intergranular cracking susceptibility of cold-worked stainless steel [14,15]. Recent reviews have confirmed a correlation between hardening and intergranular cracking susceptibility for the nuclear components' low-dose irradiated commercial alloys [13,16]. Gussev, et al., reported that irradiation could induce strain-hardening behavior and ductility damage in 316L stainless steel by in situ tensile testing [17]. As previously mentioned, there are relatively limited studies on the creep properties of irradiated welded joints [18].

Nuclear fission reaction generates plenty of heat energy in nuclear power plants. At the same time, the fission reaction releases radioactive rays, and high-energy particles will seriously threaten human safety and the natural environment through gamma and accelerator radiation [19–21]. In addition, to satisfy energy demand, high-level liquid radioactive wastes are also increasing, threatening the sustainable development of nuclear energy. During the container service, irradiation damage will increase the risk of leakage of high-level liquid radioactive waste into the environment, which causes significant damage to living humans. This combination of environments can lead to irradiation-induced precipitation, segregation and embrittlement, and enhanced hardening and creep [22]. Hence, suitable simulation methods and evaluation measures must be provided in accordance with the irradiation conditions for the safe disposal process of the container. Li, et al., reported that 316L stainless steel presents a more uniform distribution of radiation defects under ion irradiation conditions [23]. However, the photoelectric effect of the gamma rays from ^{60}Co shows a sharp decrease in the stainless steel samples [24]. Medhat, et al., investigated how the gamma energy damaged the effective atomic number and electron density for oxide dispersion-strengthened steels [25]. Therefore, the effect of gamma irradiation for 310S welded joints should be further studied.

Accelerators with particle energy of several MeV or higher are extensively used in irradiation damage studies, which could achieve at least 1×10^{18} ions/m^2 within an acceptable length of time at a stabilized temperature. The investigation of the container's irradiated damage can be conducted under special conditions by the accelerators. It is possible to irradiate the container welded joints with the accelerators instead of the high-level liquid radioactive wastes. These simulation experiments aim to study the impact of irradiated damage on the welded joints. It is well known that irradiation could increase the content of dislocation, voids and precipitates, which further affect the mechanical properties [26,27]. These irradiation-induced defects can enhance the elements' segregation of materials, leading to a synergy of the effects of the irradiation damage [28]. Lin, et al., reported that irradiation significantly increases the cracking susceptibility of 308L welded joints, and causes various deformation microstructures, including lathy faulted plane, dislocation and deformation twins in austenite [29]. However, such coupling effects in the welded joints remain elusive to date. Hence, we deliberately used the 310S welded joints stainless steel for this research. Based on the ^{60}Co and accelerator simulated irradiation experiments, the peak damage regions contain the whole welded joints. Therefore, the ^{60}Co and accelerator provide an ideal method to study the irradiation damage on the mechanical properties of the whole welded joints. Based on the above survey, it is evident that no comprehensive analysis was reported to compare the effect of irradiation damage

on microstructure evolution, and mechanical property performance of 310S welded joints in simulation.

In this study, the irradiation-induced microstructure evolution and mechanical properties degradation of the 310S stainless steel welded joints were studied by ^{60}Co and accelerator for simulating irradiation damage, which is a fairly good simulation of the irradiation damage generated in the high-level liquid radioactive wastes. The mechanical properties degradation was studied by using tensile test, creep test and Nano-indentation. The microstructure evolution and elements segregation on the specimens' surface were characterized using electron back scattered diffraction (EBSD) and atom probe tomography (APT), respectively. The dominant factors affecting the ductility and cracking along the grain boundary were discussed based on the analysis of the element's segregation and cracking tendency.

2. Experiment

2.1. Specimen Preparation and Heat Treatments

The austenitic stainless steel base metal has undergone a solution treatment at 1050 °C for 20 min, followed by final water quenching. The 6.5 mm thick 310S butt welded joint was obtained by plasma arc welding (PAW), and the filler material is 25Cr-20Ni welding wires with a diameter of 1.2 mm. The main chemical compositions of the base metal (BM) and filler materials are listed in Table 1. The welding parameters are given in Table 2. The following calculation equation for the heat input Q was used:

$$Q = \eta \frac{I \times U}{V} \quad (1)$$

where, I is welding current; U is welding voltage; ν is welding speed; η is welding thermal efficiency, and the value is 0.6. The calculated heat input Q is 0.8 KJ/mm.

Table 1. The main chemical compositions of BM and filler materials (wt.%).

Elements	C	Cr	Ni	Mn	Mo	Si	Co	Nb	N	Ce	Ta	Fe
BM	0.10	20.5	11.1	2.0	0.05	2.20	0.10	0.03	/	0.04	/	Bal.
Filler materials	0.09	26.4	21.8	2.0	0.35	0.38	0.20	0.05	0.15	/	0.20	Bal.

Table 2. PAW welding parameters for 310S stainless steel.

Welding Current (A)	Welding Voltage (V)	Welding Speed (mm/s)	Gas Flow Rate (L/min)	Groove Type	Groove Gap (mm)
160	25	3	15	I	0–0.1

2.2. Irradiation Experiments

The specimens with a dimension of 80 mm × 20 mm × 3 mm were taken down from the 310S welded joints, and the weld metal (WM) was in the middle. The specimens were ground with sandpapers up to 2000 # grit for irradiation experiments to obtain uniform damage on the specimen surface. Then the specimen was exposed to a 50 nm colloidal silica slurry polisher for over 2 h to produce a surface free of residual strain prior to the irradiation experiment. At last, all specimens were irradiated by Gamma ray (γ) of 1.2 MeV at room temperature using the ^{60}Co radioactive sources up to 5×10^7 Gy. Half of the specimens were taken out to continue the irradiation experiment by electron of the GJ-2 accelerator at Sichuan Institute of Atomic Energy, up to 1×10^8 Gy. In order to prevent radiation damage to the human body, radiation experiments were conducted in specific rooms equipped with lead plates. The absorbed dose was calculated with a potassium dichromate working dosimeter. The irradiated specimens obtained a nearly uniform damage profile with the 3 mm thick damage by the ^{60}Co irradiation, and irradiation damage extends to a

maximum depth of about 0.5 mm from the specimens' surface by the accelerator irradiation, respectively. Following the irradiation, the irradiated specimens were polished again with the 50 nm diamond paste for about 1 h to obtain fresh surfaces. This removed the surface with a thickness of 10 μm and could ensure that the specimen surfaces following different irradiation doses were consistent.

2.3. Tensile and Creep Tests

The tensile specimens with a dimension of 58 mm × 14 mm × 3 mm were taken down from the 310S welded joints based on the GB/T 228.1-2021 standard [30]. The tensile tests were performed at room temperature and 600 °C, respectively. The tests were then performed under a 1.6 mm/min strain by TSE503C tensile tests machine (Wance Co., Ltd, Shanghai, China). According to the GB/T 2013-2012 standard [31], standard creep specimens were tested by the CRITM uniaxial creep test machine (CRITM Co., Ltd, Changchun, China). According to EN 10095-2012 standard [32], the interrupted creep tests and creep rupture tests were conducted under different stress at 600 °C, respectively 170 MPa and 238 MPa. The standard specimen sizes of the tests are shown in Figure 1. In order to ensure the reproducibility of the experiments, two microstructure samples and three mechanical property samples were tested in this study. The effect of irradiation on mechanical properties was analyzed by comparing the stress-strain curves and creep deformation behavior of the unirradiated specimens with that of the different irradiated ones. During the creep test, the interrupted creep deformation and creep fracture were studied at 170 MPa and 238 MPa, respectively. The creep test for half of the specimen was interrupted at 1000 h to study the creep deformation; the other half was until fracture failure to study the fracture behavior. In addition, the fracture morphology was observed by using SEM in order to analyze the characteristics of the irradiation specimens.

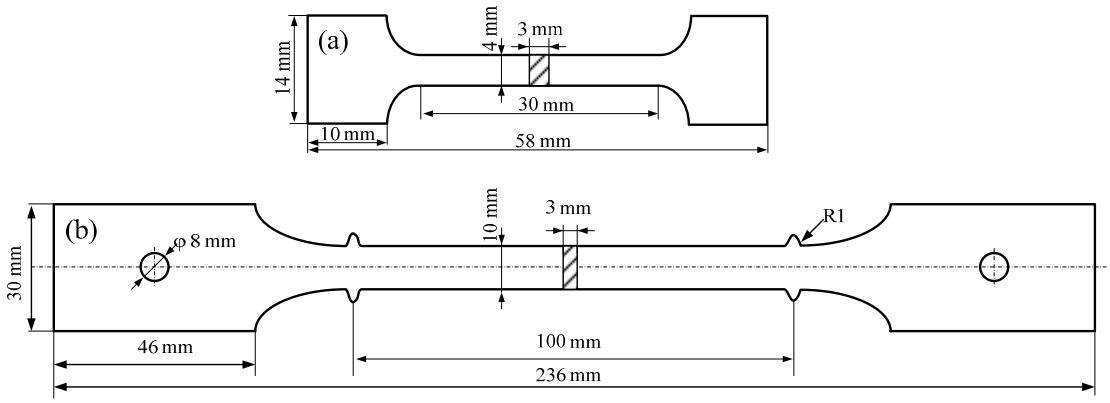

Figure 1. (**a**) Dimension of tensile specimens; and (**b**) dimension of creep specimens.

3. Experimental Results and Analysis

3.1. Tensile Property

The stress-strain curves of unirradiated and irradiated 310S stainless steel welded joints at different temperatures are shown in Figure 2. A ductility-decreased phenomenon was formed on the irradiated specimen, while excellent mechanical properties were observed on the irradiated specimen. In comparison, the effect of irradiation on the plastic properties of 310S welded joints was more evident at 600 °C. The irradiation hardening of 310S welded joints was slightly increased, and the elongation decreased of irradiated by ^{60}Co; the elongation reduction is about 5%. The stress-strain curve shows a zigzag fluctuation, which indicates welded joints occur dynamic strain ageing (DSA) at 600 °C. The DSA phenomenon may induce an additional hardening [33]. However, elongation recovery of 310S welded joints was observed by irradiation of the GJ-2 accelerator (Pioneer Electric Machine Factory, Shanghai, China). This seems to relate to the thermal effect of the high energy beam electron by the GJ-2 accelerator. All irradiation specimens exhibit a significant radiation-

induced decrease in elongation and strain hardening capacity. The elongation and strain hardening capacity reductions involve flow localization and strain hardening exhaustion mechanisms [34,35]. Excluding the decreased elongation, irradiation damage also decreases fracture toughness. The potential for irradiation damage-induced embrittlement has been paid close attention, because this phenomenon will threaten nuclear service safety.

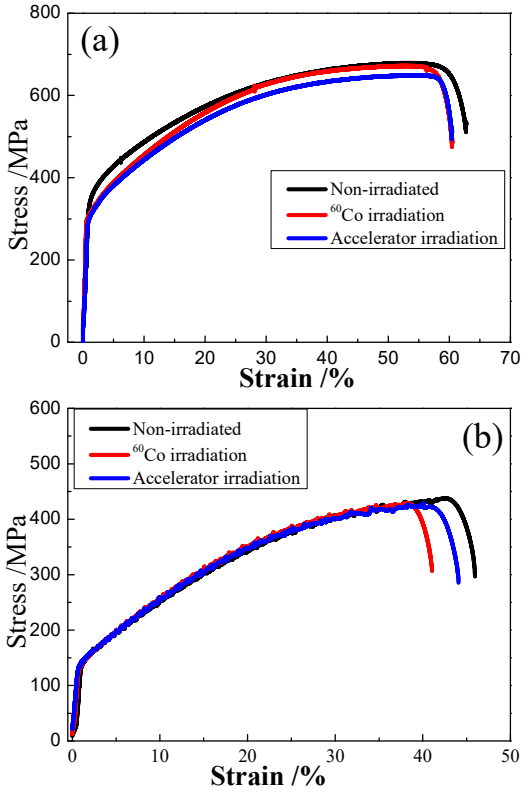

Figure 2. The stress-strain curve of tensile test: (**a**) Room temperature; and (**b**) 600 °C.

The representative fracture morphology of tensile samples at 600 °C from the unirradiated and irradiated specimens is shown in Figure 3. As mentioned above, excellent mechanical properties were found on the unirradiated specimen. The fracture morphology of unirradiated specimens shows many dimples in Figure 3a,d. However, it is seen from Figure 3b,e that the fracture morphology of the irradiated by ^{60}Co, shows a large number of secondary cracks on the surface. The secondary cracks can be due to irradiated hardening. With increasing the stress-strain in the tensile process, the micro-cracks nucleated near the hardening zone exceed the plastic deformation of the welded joints. These micro-cracks coalesce with each other to form cracks during the tensile tests. Eventually, micro-cracks proliferate and generate macro-cracks, resulting in secondary cracks on the specimen irradiated by ^{60}Co. In comparison, the fracture morphology of the irradiated by the accelerator is shown in Figure 3c,f. The dimples and voids reappeared on the fracture morphology of the irradiated specimen by the accelerator. The specimens irradiated by the accelerator revealed toughness recovery in fracture characteristics.

3.2. Creep Property

To detect the effect of irradiation on the creep property of the 310S welded joints, the deformation and creep rupture life was tested under the uniaxial tensile stress from 170 MPa to 238 MPa at 600 °C, as shown in Figure 4. The interrupted creep tests of the irradiated specimens were performed at 600 °C up to 1000 h of time at 170 MPa to detect creep deformation. The creep deformation of specimens irradiated by ^{60}Co is increased to 1.5 times that of un-irradiated specimens, indicating that irradiation-induced creep resistance decreased by ^{60}Co irradiation. Furthermore, the creep rupture tests were

further conducted at 600 °C under stresses of 238 MPa. The irradiation damage seriously degrades the creep fracture ductility of 310S welded joints. The creep fracture deformation value irradiated by ^{60}Co is reduced to 70 percent of that of unirradiated specimens. The irradiation-induced ductility damage will increase the brittle cracking tendency of welded joints. However, the accelerator irradiation specimen shows ductility recovery. The creep tests results show the same phenomenon as the tensile tests.

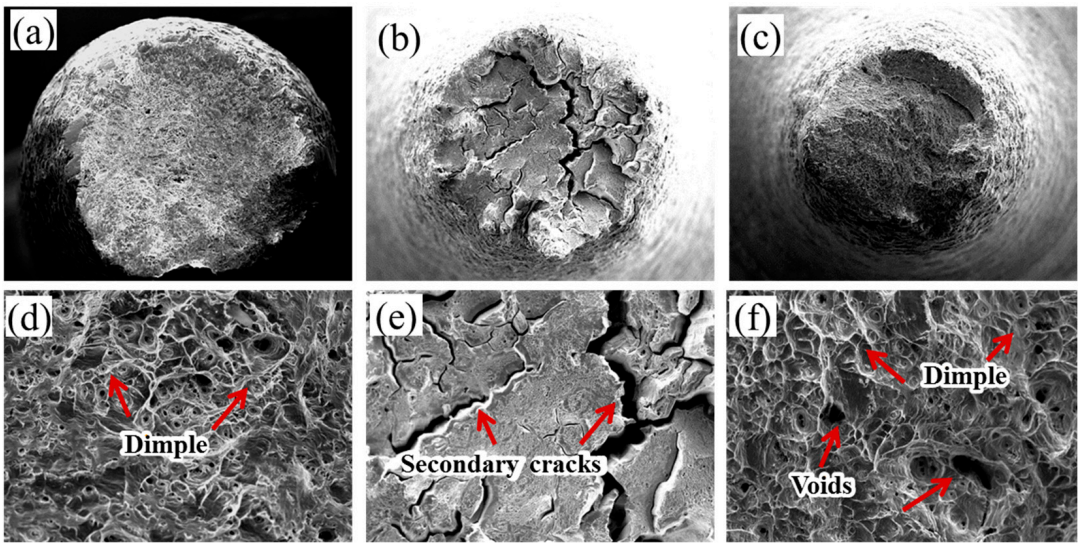

Figure 3. Fracture morphology of the un-irradiated (**a**,**d**), irradiated by ^{60}Co (**b**,**e**) and irradiated by accelerator (**c**,**f**).

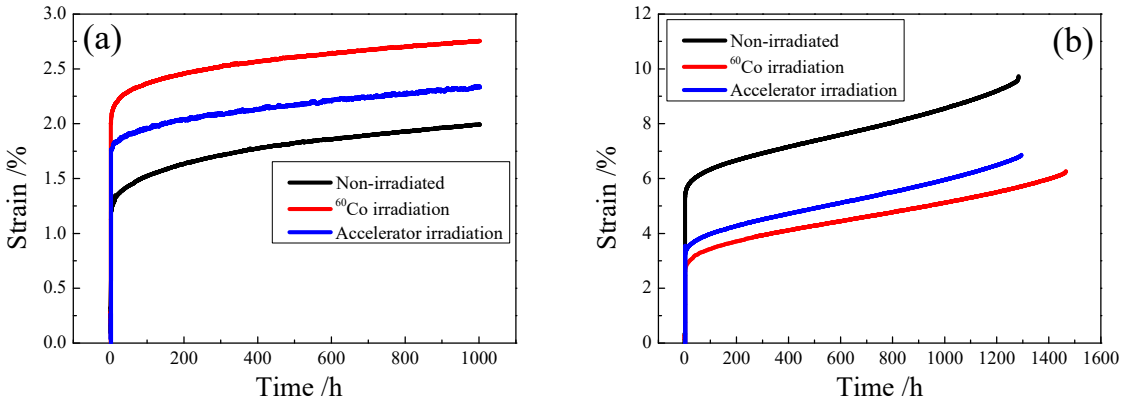

Figure 4. The creep curve of welded joints at different stress: (**a**) interrupted creep deformation at 170 MPa until 1000 h; and (**b**) creep rupture life at 238 MPa.

Figure 5 shows the creep fracture morphology of 310S welded joints specimen at 600 °C. Dimples were partially observed on the creep fracture surfaces in most of the specimens. Grain boundary fractures were observed in the ^{60}Co irradiated specimen. However, the specimens irradiated with the accelerator did not observe the grain boundary fracture. Instead, large dimples appeared, representing the toughness characteristic of the fracture morphology irradiation with the accelerator, although little voids were observed on the surfaces. The irradiation damage results in a decrease in the plasticity deformation of grains, which is one reason for the welded joints' brittleness. Moreover, the irradiation damage inhibits creep plasticity deformation, and the extent of ductility decreased obviously in the irradiated specimens with ^{60}Co.

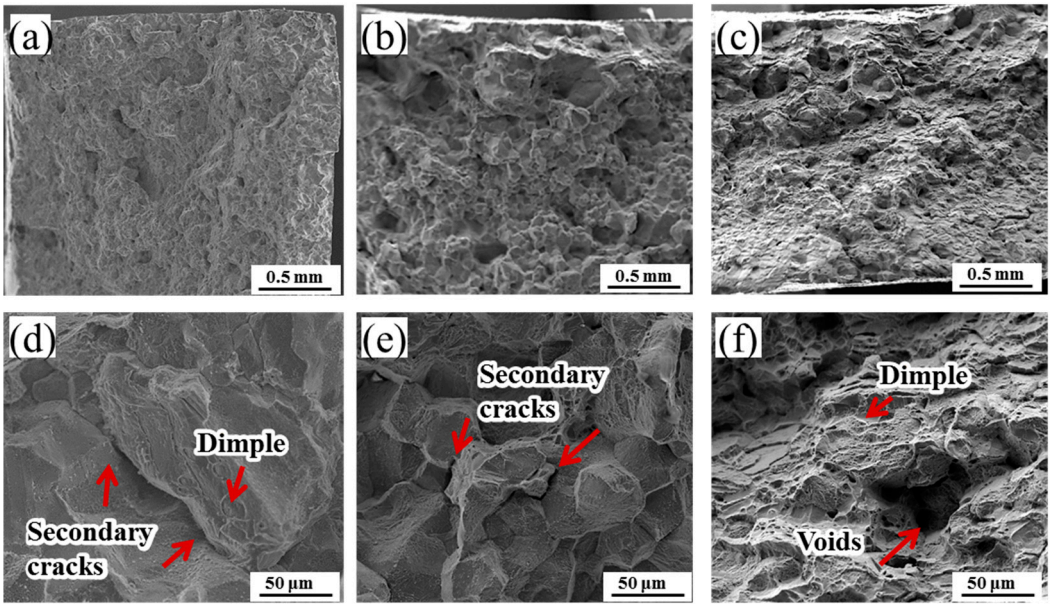

Figure 5. The fracture morphology of creep test un-irradiated (**a**,**d**), irradiated by ^{60}Co (**b**,**e**) and irradiated by accelerator (**c**,**f**).

3.3. Nano-Indentation Test

To measure the mechanical properties of a local area subjected to irradiation damage, Nano-indentation was employed to estimate the irradiation hardening on the 310S welded joints. Figure 6 shows the Nano-indenter hardness results of the specimen by ^{60}Co irradiation and electron irradiation, respectively. From the nano-indentation results, irradiation-induced hardening was observed in the 310S welded joints based on the displacement-load curve. The Nano-indenter hardness of the ^{60}Co irradiated specimens was 5.9 GPa, 44% higher than the unirradiated specimens for the base metal. In comparison, the indenter hardness decreased to 4.8 GPa by accelerator irradiation in base metal. The hardness-reduced phenomenon agrees well with recent studies in which the irradiation hardening recovery by annealing treatment [36,37]. Furthermore, the hardness increment can be attributed to radiation-induced defects and microstructure evolution [38].

3.4. APT Analysis

For further investigation of the elements segregation induced by the ^{60}Co and accelerator irradiation, atom probe tomography (APT) specimens that contain different phase boundaries were fabricated using a focused ion beam (FIB). The sample was acicular; its maximum size was about 25 nm × 25 nm × 200 nm. IVAS Standard software (TM 3.6.8, Ametek Inc., Paris, France) was used to analyze the data of elements.

The element-specific 3D point cloud atomic reconstruction results of unirradiated and irradiated specimens are shown in Figure 7. It is shown that a high density of Cr-C clusters formed near the grain boundary for the irradiated specimens. In addition, the depletion of Fe and Ni and enrichment of Cr, C and P at both phase boundaries were observed after the ^{60}Co and accelerator irradiation. However, the unirradiated specimens had no evident element clustering behavior in the welded joints.

In order to quantitatively analyze one-dimensional elements distribution, composition profiles across the phase boundary of different irradiation conditions were shown in Figure 8 for Fe, Cr, Ni, C and P, respectively. The concentration profile indicates element segregation of Cr, C and P; the element segregation degree was about 4 times, 20 times and 5 times the content of the austenite matrix, respectively, for ^{60}Co irradiation specimens. The minimum content of Cr was about 8.2 at. % at depletion on the zone of phase boundaries. The width of the Cr transition at both boundaries was approximately 6 nm. The minimum and maximum in the C-transition at both phase boundaries was 0.52 at. % and 10.7 at. %,

respectively. However, the C-transition regions showed a narrow width of approximately 4 nm. A similar width of fluctuation of P at both phase boundaries indicates similar C enrichment at both phase boundaries. With respect to the Fe depletion, the minimum Fe content at the phase boundary (about 22 at. %) was much lower than that at the matrix (about 67 at. %). With regard to the Fe depletion, the maximum P content at the phase boundary (about 0.21 at. %) was much higher than that at the matrix (about 0.03 at. %).

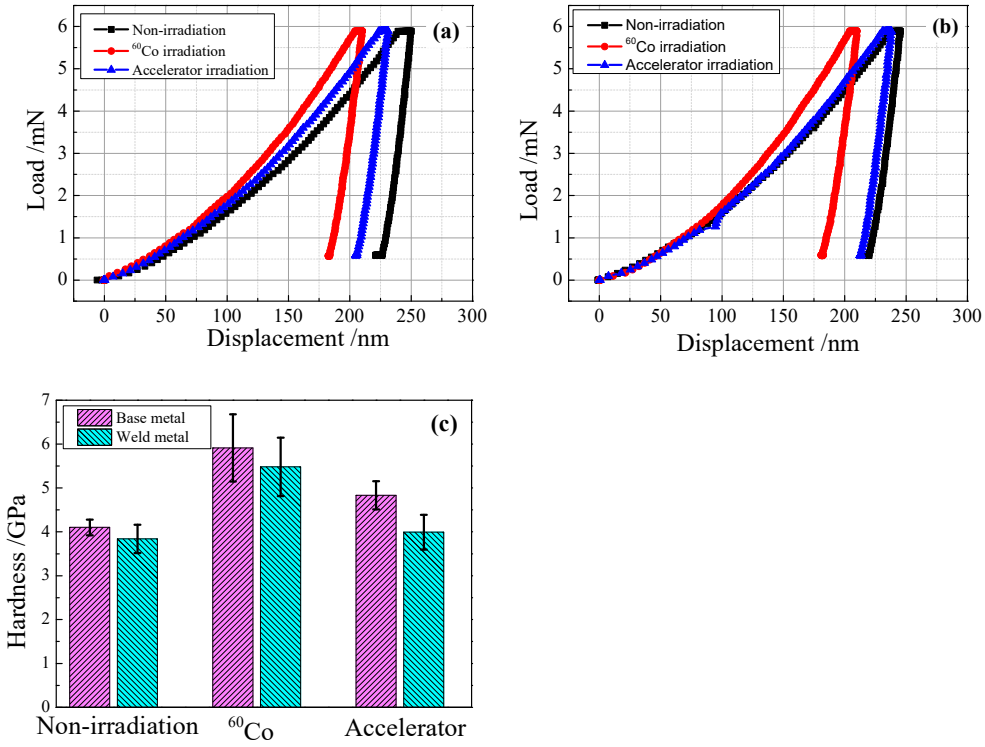

Figure 6. Results of Nano-indenter hardness: (**a**) curve of base metal; (**b**) curve of welded metal; and (**c**) hardness of welded joint.

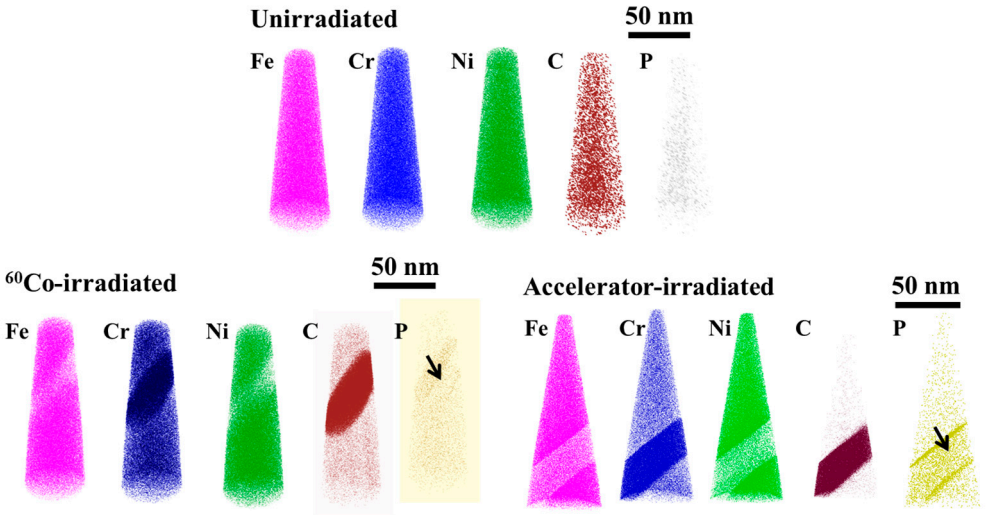

Figure 7. Atom maps of un-irradiated, ^{60}Co irradiated and accelerator irradiated samples containing a phase boundary. The arrows location was the analysis position of one-dimensional elements.

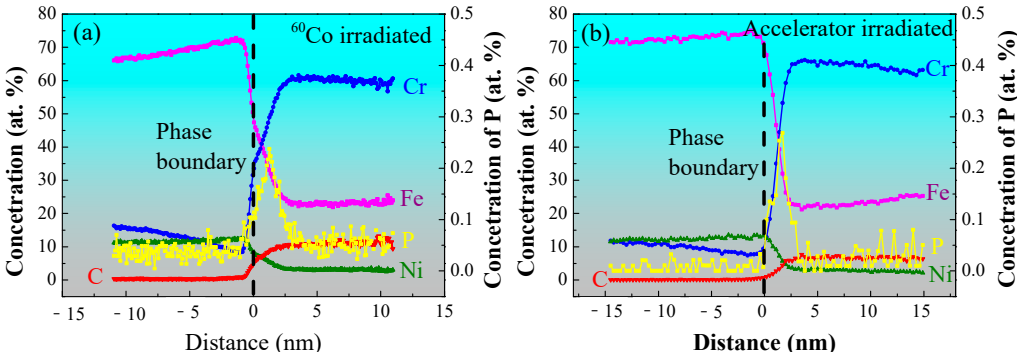

Figure 8. Composition profiles of Fe, Cr, Ni, C and P across phase boundaries: (**a**) ^{60}Co irradiated and (**b**) accelerator irradiated samples containing a phase boundary.

The element profiles were further analyzed of the accelerator composite irradiation specimens. The degree of element segregation of Cr, C and P was further aggravated and increased to about 6 times, 30 times and 8 times the content of austenite matrix for accelerator irradiation specimens. The Cr depletion at phase boundaries indicated minimum content of about 7.3 at. %, as shown in Figure 8. The width of the Cr transition at both boundaries was increased to approximately 7.5 nm. The minimum and maximum in the C transition at both phase boundaries was 0.15 at. % and 7.6 at. %, respectively. At the same time, the C transition region's width increased to approximately 4.5 nm. With respect to the Fe depletion, the minimum Fe content at the phase boundary (about 21 at. %) was much lower than that at the matrix (about 71 at. %). With regard to the Fe depletion, the maximum P content at the phase boundary (about 0.26 at. %) was much higher than that at the matrix (about 0.03 at. %). The enrichment of P appears in the phase boundaries. Compared with the ^{60}Co irradiation damage, the width and degree of element segregation increased with the accelerator combination irradiation damage. Figures 7 and 8 indicate the irradiation-induced depletion of Cr and enrichment of C and P at the phase boundaries of the austenitic matrix. As expected, element segregations are detected in the grain boundary due to irradiation; therefore, forming these detrimental structures usually leads to crack initiation during the original stage of the creep process [39].

3.5. Microstructures of Welded Joints

3.5.1. Microstructural Evolution of Welded Joints

EBSD analysis was performed with the same creep test of 238 MPa under different irradiation conditions to verify the above phenomenon further. The image quality (IQ) mappings and kernel average misorientation (KAM) superimposed maps were analyzed by electron backscatter diffraction (EBSD) for unirradiated, ^{60}Co irradiated and accelerator irradiated samples (shown in Figure 9). It is shown that the twin grains (TBs) microstructure has a larger strain in base metal for the irradiated specimens in Figure 9. In the present study, it can be reasonably assumed that the process of twin microstructure during plastic deformation largely generates the interaction between dislocations and TBs, mainly driven by the accumulation of plastic strain during the creep deformation [40,41]. When we further compare the superimposed maps of the welded joints at various conditions, it can be found that the local misorientation becomes remarkable at the grain boundary of irradiation specimens. This phenomenon conforms to the hypothesis that the mechanism of the sub-grains was combined through the loss of grain diversity. Moreover, the irradiation microstructures were not found in TBs microstructure. Therefore, KAM maps could provide detailed information on strain accumulation as a function of crystal orientation. The local misorientation of irradiation specimens was lower than that of unirradiated specimens from the KAM maps. At the same time, it is observed that the irradiation specimen shows a mass of large angle grain boundaries, which is consistent with the phenomenon of creep fracture deformation decreased for irradiation specimen. It can be observed in this study

that the cracks mainly initiate at the grain boundary due to the element segregation and hardening not being well-compatible at deformation. With further creep straining, the cracks propagated along the weakened grain boundaries, leading to the secondary cracks on the fracture morphology in Figure 5. Therefore, element segregation and hardening should be carefully concerned to analyze irradiation damage. In addition, the evenly distributed precipitated phase will reduce the micro-cracks propagation along the grain boundary.

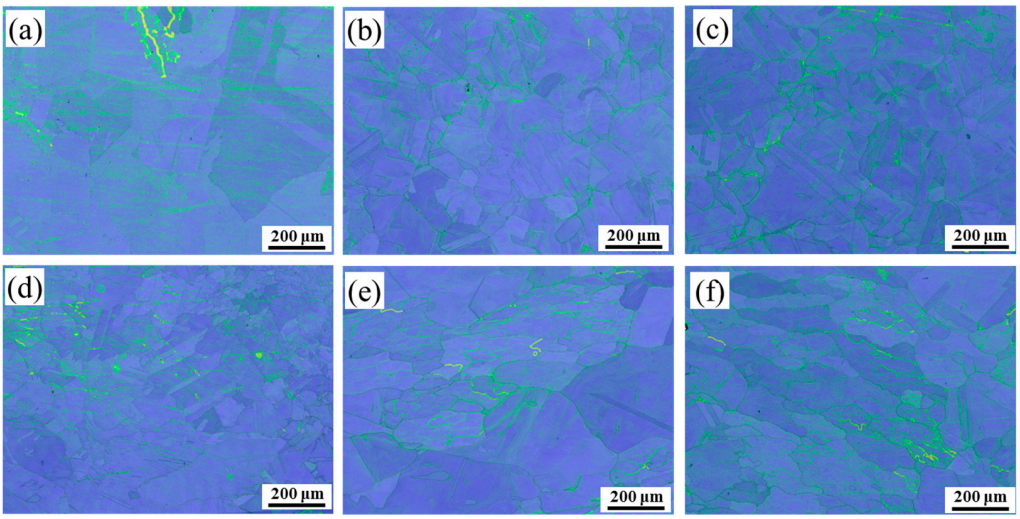

Figure 9. Image quality (IQ) mapping superimposed with kernel average misorientation (KAM) mapping of base metal (**a**–**c**), weld metal (**d**–**f**) of the weld joints: un-irradiated (**a**,**d**), irradiated by ^{60}Co (**b**,**e**) and irradiated by accelerator (**c**,**f**).

The welded joints grain analysis of unirradiation and irradiation was conducted to clarify the microstructure evolution during the irradiation experiments, as shown in Figure 10. The base metal of the un-irradiation mainly comprised sub-grains with small, recrystallized grains, as shown in Figure 10a,d. However, the irradiation samples were mainly recrystallized grains (about 80%). The recrystallization frication of welded joints increases obviously in irradiation specimens. The recrystallization process will cause lattice distortion of adjacent grains, and grain boundaries will be fractured, resulting in internal stress between grains in severe cases. At the same time, the welded joints will have premature creep fracture under the effect of external stress.

3.5.2. Irradiation-Induced Cracking Behavior

The ^{60}Co irradiation-induced microstructure evolutions in the welded joints have affected the mechanical properties. Then, the cracking behaviors were analyzed from irradiated welded joint specimens. Afterwards, the cracking mechanism was characterized based on the results of SEM and EBSD. The location of cracks, phase distribution, KAM and element segregation are shown in Figure 11. Some intergranular cracks are observed on the virgin surface of the ^{60}Co irradiated specimen in Figure 11a. Then, specific cracks were analyzed by IQ mapping. The grain boundaries appeared to have a larger strain than the austenite matrix in Figure 11b. Further, it can be seen from Figure 11c that the brittle phase of $M_{23}C_6$ and δ-ferrite along the intergranular cracks, especially near the cavities, is where the microstructure features were noticeable. It should be noted that the emersion of $M_{23}C_6$ and δ-ferrite could deteriorate the toughness properties of the welded joints. Therefore, the cavities nucleate around the carbides due to the inharmonious deformation resistance between the low stability $M_{23}C_6$ and matrix. During the initiation of the creep process, the cavities are propagated and extended into cracks along the grain boundary, where they separate from discontinuous $M_{23}C_6$. Discontinuous $M_{23}C_6$ and δ-ferrite would affect the creep strain of the irradiated specimen by ^{60}Co; the KAM is shown in Figure 11d. The grain boundary shows higher KAM values (0.90°), indicating

a greater crystallographic orientation, resulting in inharmonious deformation during the creep. Therefore, the nucleation of cavities along the grain boundary is accelerated in the creep process. At the same time, the element enrichment of C and Cr was observed along the grain boundary, as shown in Figure 11e,f. Wang, et al., reported that precipitates contribute to promoting the generation of creep cracks near the grain boundary [42]. Finally, intergranular cracks lead to intergranular fracture of the 310S welded joint.

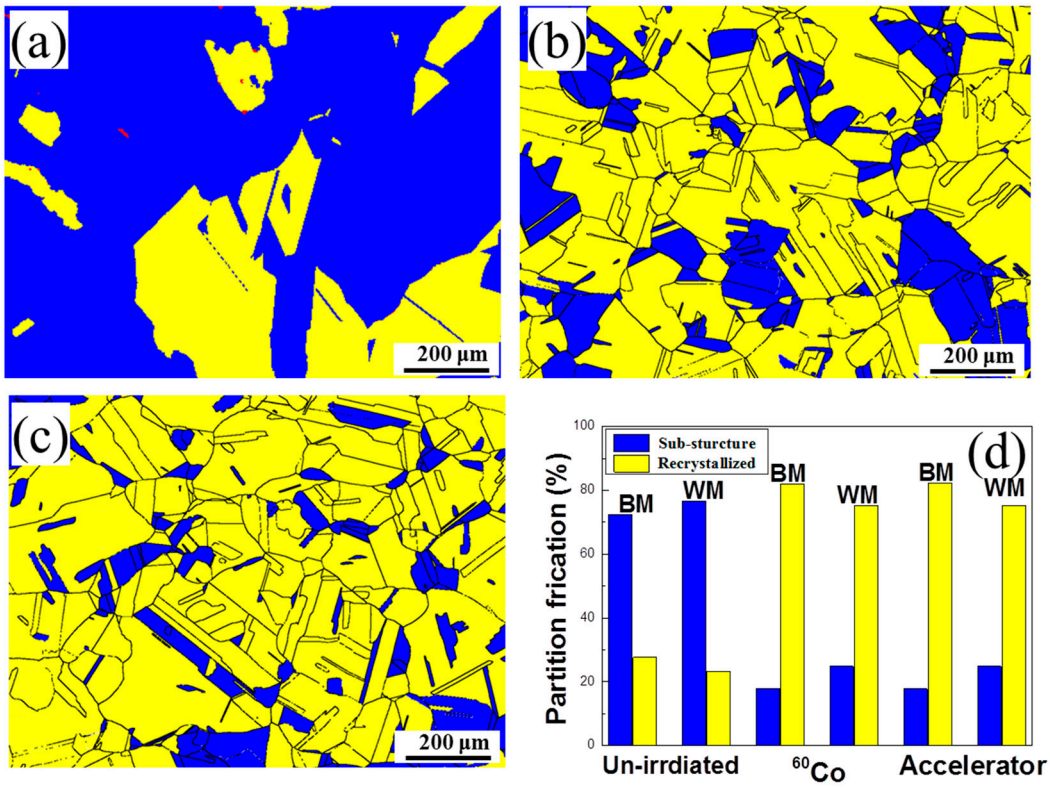

Figure 10. Figure 10. Grain orientation spread maps of base metal: (**a**) un-irradiated, (**b**) irradiated by ^{60}Co and (**c**) irradiated by accelerator, and (**d**) fraction of recrystallized and sub-structured in various specimens.

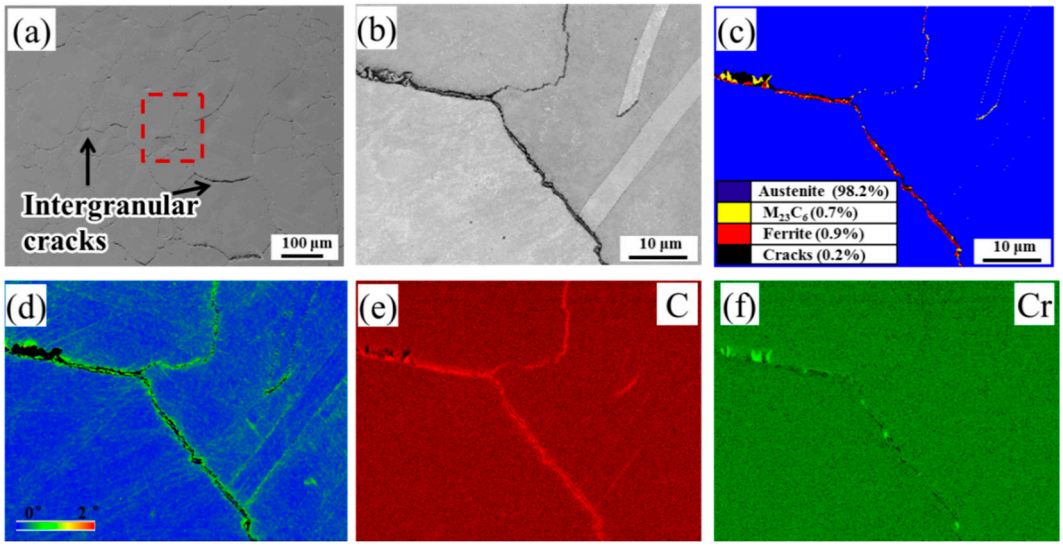

Figure 11. Microstructure near creep rupture of ^{60}Co irradiated samples: (**a**) cavities; (**b**) image quality (IQ); (**c**) phase distribution; (**d**) phase distribution of kernel average misorientation (KAM); (**e**) C element distribution and (**f**) Cr elements distribution.

Recent studies of the cracking initiation of austenitic stainless steel have an increasing relevance of the role of irradiation damage [43,44]. These studies have shown that discontinuous cavities intersected grain boundaries have a higher fraction of crack initiation, and this inharmonious strain between adjacent grains enhanced cracking fraction is likely due to the high stress at the intersections [45]. Furthermore, this increase in stress has been linked to the heap up of the dislocation near the grain boundary after moving through the cavities and dislocation band [46]. It should also be noted that triple boundaries also had a similarly high cracking fraction as these locations experience high-stress concentration.

Regarding the ^{60}Co irradiation specimen, a good correlation is observed between cracking susceptibility and element segregation; cracking susceptibility increases with element segregation. Cracking along the grain boundary phenomenon was observed for the irradiation specimen, showing the highest degree of element segregation in the grain boundary. On the other hand, the cracking behavior of ^{60}Co would lead to the conclusion that a certain amount of hardening in the irradiated damage specimen can conduct to increase the cracking susceptibility. The lowest creep fracture deformation was observed for the ^{60}Co irradiation specimen, which also shows the highest hardening.

In this study, we have confirmed the connection between irradiation damage and the mechanical properties of the 310S welded joint. Irradiation damage caused a reduction in plastic parameters in the tensile and creep tests, likely due to irradiation-induced hardening and element segregation. An investigation of the crack behavior for this study showed that crack initiation sites were related to $M_{23}C_6$ and δ-ferrite, with heterogeneous deformation and high-stress concentration. However, this does not discuss the cracking behavior of the two-irradiation test, because the cracking behavior was similar. We will explore ways to eliminate irradiation damage for 310S welded joints in the following research.

4. Conclusions

In order to investigate the effect of irradiated damage on glass solidification of high-level liquid radioactive waste, the microstructure evolution and mechanical properties of the 310S stainless steel welded joints under ^{60}Co and accelerator irradiation were investigated. As a result, the conclusions could be drawn as follows:

(1) The elongation and creep properties decreased for irradiation specimens, especially the elongation reduction reaching about 5%, and the creep fracture deformation value was reduced to 70% that of un-irradiated specimens by ^{60}Co. The specimens of mechanical properties revealed recovery for irradiated specimens by the accelerator;
(2) The ^{60}Co irradiated specimens had the highest Nano-indenter hardness, especially the hardness of base metal was 5.9 GPa, 44% higher than the unirradiated specimens. On the other hand, the indenter hardness decreased after the accelerator irradiation;
(3) The irradiation-induced Cr, C and P enrichment at the phase boundaries for ^{60}Co irradiation specimens. After further accelerator irradiation, the degree of element segregation is further intensified; the width of the Cr transition at both boundaries was increased from 6 nm to 7.5 nm;
(4) Based on element segregation analysis, irradiation-induced element segregation forms rich Ni and Si enrichment and Cr depletion at grain boundaries and precipitates. Under the action of continuous tensile stress, cavity defects are easily formed between $M_{23}C_6$ carbide and the non-coherent austenite matrix. The growth of cavities will accumulate the intergranular cracks nucleation, leading to intergranular fracture for welded joints.

Author Contributions: Conceptualization, Y.J.; methodology, Y.J.; validation, Y.J. and Y.K.; formal analysis, Y.J.; investigation, Y.J.; resources, H.C.; data curation, Y.J.; writing—original draft preparation, Y.J.; writing—review and editing, Y.K., C.W. and H.C.; supervision, H.C.; project administration, H.C.; funding acquisition, Y.J. and H.C. All authors have read and agreed to the published version of the manuscript.

Funding: This research was funded by 2020 LingChuang Research Project of China National Nuclear Corporation.

Data Availability Statement: The data presented in this study are available on request from the corresponding author.

Acknowledgments: The authors would like to acknowledge the financial support provide by the project of 2020 LingChuang Research Project of China National Nuclear Corporation. The authors also wish to acknowledge the supply of the stainless steel and welded joint samples from China Erzhong Group Co., Ltd., Deyang, China.

Conflicts of Interest: The authors declare no conflict of interest.

References

1. Kearney, S.; Yorkshire, A.S.; Geddes, D.A.; Hanein, T.; Nelson, S.; Provis, J.L.; Walkley, B. Chapter 25—Cement-based stabilization/solidification of radioactive waste. In *Low Carbon Stabilization and Solidification of Hazardous Wastes*; Tsang, D.C.W., Wang, L., Eds.; Elsevier: Amsterdam, The Netherlands, 2022; pp. 407–431.
2. Tan, S. Chapter 26—Glass-based stabilization/solidification of radioactive waste. In *Low Carbon Stabilization and Solidification of Hazardous Wastes*; Tsang, D.C.W., Wang, L., Eds.; Elsevier: Amsterdam, The Netherlands, 2022; pp. 433–447.
3. Lo, K.H.; Shek, C.H.; Lai, J.K.L. Recent developments in stainless steels. *Mater. Sci. Eng. R Rep.* **2009**, *65*, 39–104. [CrossRef]
4. Liu, Z.; Lu, J.; Su, H.; Long, J.; Li, L.; Wang, P.; Cong, S.; Ma, Z.; Zhang, L.; Guo, X. On the role of mechanical deformation in the environmental degradation of 310S stainless steels in supercritical carbon dioxide. *Corros. Sci.* **2022**, *207*, 110537. [CrossRef]
5. Ustrzycka, A. Physical Mechanisms Based Constitutive Model of Creep in Irradiated and Unirradiated Metals at Cryogenic Temperatures. *J. Nucl. Mater.* **2021**, *548*, 152851. [CrossRef]
6. Paccou, E.; Tanguy, B.; Legros, M. Irradiation-assisted stress corrosion cracking susceptibility and mechanical properties related to irradiation-induced microstructures of 304L austenitic stainless steel. *J. Nucl. Mater.* **2020**, *528*, 151880. [CrossRef]
7. Jepeal, S.J.; Danagoulian, A.; Kesler, L.A.; Korsun, D.A.; Lee, H.Y.; Schwartz, N.; Sorbom, B.N.; Lopez, E.V.; Hartwig, Z.S. An accelerator facility for intermediate energy proton irradiation and testing of nuclear materials. *Nucl. Instrum. Methods Phys. Res. Sect. B Beam Interact. Mater. At.* **2021**, *489*, 41–49. [CrossRef]
8. Fukuya, K.; Nishioka, H.; Fujii, K.; Kamaya, M.; Miura, T.; Torimaru, T. Fracture behavior of austenitic stainless steels irradiated in PWR. *J. Nucl. Mater.* **2008**, *378*, 211–219. [CrossRef]
9. Kenik, E.A.; Busby, J.T. Radiation-induced degradation of stainless steel light water reactor internals. *Mater. Sci. Eng. R Rep.* **2012**, *73*, 67–83. [CrossRef]
10. Chopra, O.K.; Rao, A.S. A review of irradiation effects on LWR core internal materials—Neutron embrittlement. *J. Nucl. Mater.* **2011**, *412*, 195–208. [CrossRef]
11. Bosch, R.W.; Vankeerberghen, M.; Gérard, R.; Somville, F. Crack initiation testing of thimble tube material under PWR conditions to determine a stress threshold for IASCC. *J. Nucl. Mater.* **2015**, *461*, 112–121. [CrossRef]
12. Wang, S.; Zhang, S.; Xie, J.; Feng, X.; Song, M.; Was, G.S.; Kuang, W. Clarifying the mitigation effect of proton irradiation on the intergranular oxidation of 316L stainless steel in high temperature water. *Acta Mater.* **2022**, *241*, 118408. [CrossRef]
13. Liang, D.; Hure, J.; Courcelle, A.; El Shawish, S.; Tanguy, B. A micromechanical analysis of intergranular stress corrosion cracking of an irradiated austenitic stainless steel. *Acta Mater.* **2021**, *204*, 116482. [CrossRef]
14. Féron, D.; Herms, E.; Tanguy, B. Behavior of stainless steels in pressurized water reactor primary circuits. *J. Nucl. Mater.* **2012**, *427*, 364–377. [CrossRef]
15. Pokor, C.; Brechet, Y.; Dubuisson, P.; Massoud, J.-P.; Averty, X. Irradiation damage in 304 and 316 stainless steels: Experimental investigation and modeling. Part II: Irradiation induced hardening. *J. Nucl. Mater.* **2004**, *326*, 30–37. [CrossRef]
16. Wang, M.; Song, M.; Lear, C.R.; Was, G.S. Irradiation assisted stress corrosion cracking of commercial and advanced alloys for light water reactor core internals. *J. Nucl. Mater.* **2019**, *515*, 52–70. [CrossRef]
17. Gussev, M.N.; McClintock, D.A.; Lach, T.G. Origin, parameters, and underlying deformation mechanisms of propagating deformation bands in irradiated 316L stainless steel. *Acta Mater.* **2023**, *242*, 118434. [CrossRef]
18. Fuller, R.W.; Simsiriwong, J.; Shamsaei, N. Crack growth prediction for irradiated stainless steels under the combined fatigue-creep loading. *Theor. Appl. Fract. Mech.* **2020**, *109*, 102759. [CrossRef]
19. Aygün, B. High alloyed new stainless steel shielding material for gamma and fast neutron radiation. *Nucl. Eng. Technol.* **2020**, *52*, 647–653. [CrossRef]
20. Kumar, P.; Soni, R.K.; Dehiya, B.S.; Sivakumar, V.V. Study of phase changes induced by gamma irradiation in welded stainless steel alloys 304 and 316. *Mater. Today Proc.* **2021**, *47*, 6545–6550. [CrossRef]
21. Aygün, B. Neutron and gamma radiation shielding Ni based new type super alloys development and production by Monte Carlo Simulation technique. *Radiat. Phys. Chem.* **2021**, *188*, 109630. [CrossRef]
22. Hoffman, A.K.; Zhang, Y.; Arivu, M.; He, L.; Sridharan, K.; Wu, Y.; Islamgaliev, R.K.; Valiev, R.Z.; Wen, H. Novel effects of grain size and ion implantation on grain boundary segregation in ion irradiated austenitic steel. *Acta Mater.* **2023**, *246*, 118714. [CrossRef]

23. Li, C.; Chen, F.; Ge, G.; Lin, J.; Sun, Z.; Fan, M.; Huang, P.; Tang, X. Impact of sub-grain structure on radiation resistance in additively manufactured 316L stainless steels: An atomic insight into the mechanism. *Appl. Surf. Sci.* **2022**, *606*, 154926. [CrossRef]
24. Eissa, M.M.; El-kameesy, S.U.; El-Fiki, S.A.; Ghali, S.N.; El Shazly, R.M.; Saeed, A. Attenuation capability of low activation-modified high manganese austenitic stainless steel for fusion reactor system. *Fusion Eng. Des.* **2016**, *112*, 130–135. [CrossRef]
25. Medhat, M.E.; Wang, Y. Investigation on radiation shielding parameters of oxide dispersion strengthened steels used in high temperature nuclear reactor applications. *Ann. Nucl. Energy* **2015**, *80*, 365–370. [CrossRef]
26. Obodovskiy, I. Chapter 29—Fundamentals of Radiation Materials Science. In *Obodovskiy I. Radiation*; Elsevier: Abingdon, UK, 2019; pp. 367–371.
27. Jiang, B.; Liang, N.; Xu, L.; Gao, L.; Peng, Q.; Jiao, Z.; Chen, Y.; Li, W.; He, Y.; Wang, L. Combined effects of irradiation and hydrogen on the mechanical and corrosion performances of the ferrite in duplex phase steels. *J. Nucl. Mater.* **2022**, *572*, 154069. [CrossRef]
28. Jiang, B.; Zhang, B.; He, Y.; Peng, Q.; Jiao, Z.; Qiao, L. Combined effects of irradiation and hydrogen ions on surface oxidation of 308 L austenite stainless steel. *Corros. Sci.* **2021**, *191*, 109734. [CrossRef]
29. Lin, X.; Peng, Q.; Han, E.-H.; Ke, W. Deformation and cracking behaviors of proton-irradiated 308L stainless steel weld metal strained in simulated PWR primary water. *J. Mater. Sci. Technol.* **2022**, *120*, 36–52. [CrossRef]
30. *GB/T 228.1-2021*; Metallic Materials—Testing Testing—Part 1: Method of Test at Room Temperature. Standards Press of China: Beijing, China, 2021.
31. *GB/T 2039-2012*; Metallic materials—Uniaxial Creep Testing Method in Tension. Standards Press of China: Beijing, China, 2012.
32. *EN 10095*; Heat Resisting Steels and Nickel Alloys. European Committee for Standardization: Berlin, Germany, 2018.
33. Yang, W.-H.; Cheng, P.-M.; Li, Y.; Wang, R.; Liu, G.; Xin, L.; Zhang, J.-Y.; Li, D.-P.; Zhang, H.-B.; Sun, J. Dynamic strain aging-mediated temperature dependence of ratcheting behavior in a 316LN austenitic stainless steel. *Mater. Sci. Eng. A* **2023**, *862*, 144503. [CrossRef]
34. Sauzay, M.; Bavard, K.; Karlsen, W. TEM observations and finite element modelling of channel deformation in pre-irradiated austenitic stainless steels—Interactions with free surfaces and grain boundaries. *J. Nucl. Mater.* **2010**, *406*, 152–165. [CrossRef]
35. Byun, T.S.; Farrell, K.; Li, M. Deformation in metals after low-temperature irradiation: Part II—Irradiation hardening, strain hardening, and stress ratios. *Acta Mater.* **2008**, *56*, 1056–1064. [CrossRef]
36. Fukumoto, K.I.; Mabuchi, T.; Yabuuchi, K.; Fujii, K. Irradiation hardening of stainless steel model alloy after Fe-ion irradiation and post-irradiation annealing treatment. *J. Nucl. Mater.* **2021**, *557*, 153296. [CrossRef]
37. Van Renterghem, W.; Al Mazouzi, A.; Van Dyck, S. Influence of post irradiation annealing on the mechanical properties and defect structure of AISI 304 steel. *J. Nucl. Mater.* **2011**, *413*, 95–102. [CrossRef]
38. Shin, J.H.; Kong, B.S.; Jeong, C.; Eom, H.J.; Jang, C.; Shao, L. Evaluation of radiation resistance of an austenitic stainless steel with nanosized carbide precipitates using heavy ion irradiation at 200 dpa. *Nucl. Eng. Technol.* **2023**, *55*, 555–565. [CrossRef]
39. Zinkle, S.J.; Was, G.S. Materials challenges in nuclear energy. *Acta Mater.* **2013**, *61*, 735–758. [CrossRef]
40. Sarkar, A.; Dash, M.K.; Nagesha, A.; Dasgupta, A.; Sandhya, R.; Okazaki, M. EBSD based studies on various modes of cyclic deformation at 923 K in a type 316LN stainless steel. *Mater. Sci. Eng. A* **2018**, *723*, 229–237. [CrossRef]
41. Yang, W.-H.; Cheng, P.-M.; Li, Y.; Wang, R.; Liu, G.; Xin, L.; Zhang, J.-Y.; Sun, J. Ratcheting-induced twinning/de-twinning behaviors in a 316LN austenitic stainless steel. *Mater. Sci. Eng. A* **2022**, *851*, 143648. [CrossRef]
42. Wang, Y.; Zhang, W.; Wang, Y.; Lim, Y.C.; Yu, X.; Feng, Z. Experimental evaluation of localized creep deformation in grade 91 steel weldments. *Mater. Sci. Eng. A* **2021**, *799*, 140356. [CrossRef]
43. Stephenson, K.J.; Was, G.S. The role of dislocation channeling in IASCC initiation of neutron irradiated stainless steel. *J. Nucl. Mater.* **2016**, *481*, 214–225. [CrossRef]
44. Jiao, Z.; Was, G.S. Localized deformation and IASCC initiation in austenitic stainless steels. *J. Nucl. Mater.* **2008**, *382*, 203–209. [CrossRef]
45. Johnson, D.C.; Kuhr, B.; Farkas, D.; Was, G.S. Quantitative analysis of localized stresses in irradiated stainless steels using high resolution electron backscatter diffraction and molecular dynamics modeling. *Scr. Mater.* **2016**, *116*, 87–90. [CrossRef]
46. McMurtrey, M.D.; Cui, B.; Robertson, I.; Farkas, D.; Was, G.S. Mechanism of dislocation channel-induced irradiation assisted stress corrosion crack initiation in austenitic stainless steel. *Curr. Opin. Solid State Mater. Sci.* **2015**, *19*, 305–314. [CrossRef]